International Journal of Control, Automation and Systems 19(9) (2021) 3199-3208
http://dx.doi.org/10.1007/s12555-020-0581-8
ISSN:1598-6446 eISSN:2005-4092
http://www.springer.com/12555

# High-precision Underwater 3D Mapping Using Imaging Sonar for Navigation of Autonomous Underwater Vehicle

**Byeongjin Kim, Hangil Joe, and Son-Cheol Yu***

**Abstract:** This study proposes a method for generating a high-precision three-dimensional (3D) map using two-dimensional (2D) sonar images from an imaging sonar installed on an autonomous underwater vehicle (AUV). The 2D sonar image sequence was analyzed pairwise to estimate the amount of displacement and used to create a 2D mosaic sonar image. The mosaic sonar map contains intensity information in a wide area and precise shape information but has no height information. To overcome this limitation, we can generate a 3D point cloud from 2D sonar image sequences. This method takes advantage of the mobility of the AUV to reconstruct the height information and partially solves the ambiguity issues in the imaging sonar's elevation angle. The height map generated from the 3D point cloud contains height information of a wide area, but the shape information is inaccurate. By fusing two maps to complement each other's imperfections, we can generate a precise 3D sonar map. This map enables the AUV to estimate the pose and recognize the surrounding environment. We verified the proposed method by conducting experiments in an indoor water tank. After placing various objects on the floor, the AUV with the imaging sonar scanned the floor and objects to generate a 3D sonar map. We analyzed the estimated AUV trajectory and the accuracy of the 3D sonar map.

**Keywords:** 3D point cloud, 3D reconstruction, sonar image registration, sonar mapping, underwater navigation.

## 1. INTRODUCTION

Mapping environments and self-localization are the essential capabilities of autonomous vehicles [1–5]. It is especially challenging for autonomous underwater vehicles (AUVs) to obtain their absolute position data in underwater environments, and recognizing their surrounding environment can help the AUVs estimate their positions [6–8]. Recognizing the environment enables AUVs to perform intelligent actions and move with more accuracy, in increasing mission efficiency [9,10]. Studies have been conducted on underwater mapping using optical camera systems over a short distance [11–13]. While optical camera systems can observe in a short distance and produce a high-resolution map, it has limited usage in dark and turbid conditions.

For underwater mapping, sonar imaging systems are a suitable alternative to optical camera systems because acoustic signals can reach long distances even in turbid and dark conditions [14,15]. Studies have been conducted to generate a wide range of maps over a long distance using kHz band sonar [16,17]. However, these studies could not provide detailed information around specific regions because of their limited resolution due to their low frequency. The imaging sonar in the MHz band can provide higher resolution sonar images than sonar in the kHz range. Therefore, the MHz band imaging sonar is suitable for AUV applications because it provides high-resolution sonar images in real-time at a high frame rate.

In many AUV applications, such as black box retrieval from aerial or maritime accidents, and inspection of underwater structures, it is found that an underwater map ranging from several meters to tens of meters is necessary. The underwater map should contain details of the local area while maintaining the coincidence of the entire area. Many sonar images acquired from a high-frequency imaging sonar enable underwater mapping by generating a mosaic map. Some studies have been conducted on the registration of sonar images of an imaging sonar [18,19]. However, the studies focused on the registration image, which provides only two-dimensional (2D) information without height information. The missing height information is one of the significant disadvantages of imaging sonar systems. There have been studies on recon-

Manuscript received August 12, 2020; revised October 27, 2020; accepted December 1, 2020. Recommended by Associate Editor Sehoon Oh under the direction of Editor-in-Chief Keum-Shik Hong. This work was supported by the National Research Foundation of Korea(NRF) grant funded by the Korea government(MSIT) (No. 2017R1A5A1014883).

Byeongjin Kim and Son-Cheol Yu are with the Department of Convergence IT Engineering, Pohang University of Science and Technology (POSTECH), 77, Cheongam-ro, Nam-gu, Pohang, Gyeongbuk, Korea (e-mails: {kbj0607, sncyu}@postech.ac.kr). Hangil Joe is with the Department of Robot and Smart System Engineering, Kyungpook National University, 80, Daehak-ro, Buk-gu, Daegu, Korea (e-mail: hgjoe@knu.ac.kr).
* Corresponding author.

structing three-dimensional (3D) information using imaging sonar [20–22] to overcome this disadvantage. These studies have two main limitations: a sparse 3D point cloud and ambiguity of shape information. These problems can cause performance degradation in underwater 3D mapping.

We proposed a generation method for high-precision 3D sonar maps by fusing a 2D mosaic sonar map and a 3D point cloud. In addition, we presented an estimation method for the position difference of the AUV using sonar image pairs. Indoor water tank experiments verified the feasibility and accuracy of the proposed method.

This paper is organized as follows: In Section 2, we describe the proposed method for generating an underwater 3D sonar map using an imaging sonar. Section 3 presents the experimental results of the proposed method. Finally, Section 4 presents the conclusion.

## 2. BASICS OF IMAGING SONAR

The imaging sonar emits multiple acoustic beams and then measures the intensity and time-of-flight (TOF) of the return beams to produce a sonar image. The acoustic beams are insonified in the azimuth direction ($\theta$) and spread in the elevation direction ($\phi$). Thus, the imaging sonar has a field of view angle in the azimuth direction and a spreading angle in the elevation direction, as shown in Fig. 1(a). The intensity value of each pixel is calculated in grayscale using the range value ($r$), the TOF value, and the sound's velocity.

Because the imaging sonar's acoustic beams are spread out along the azimuth direction, the sonar image of the observation area after the interpolation process is a fan-shaped, as shown in Fig. 1(b). The original data of the sonar image without the interpolation process is presented in a rectangular matrix, as shown in Fig. 1(c). The pixel values of this matrix are intensity values that were measured based on each pixel's corresponding $r$ and $\theta$ values.

The 3D point $P_{3D}$ $(r, \theta, \phi)$ of the spherical coordinates can be expressed in Cartesian coordinates as follows:

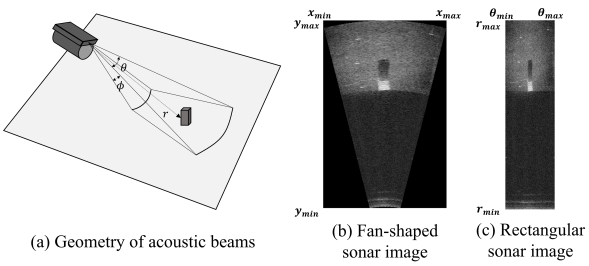


(a) Geometry of acoustic beams (b) Fan-shaped sonar image (c) Rectangular sonar image

Fig. 1. Configuration of imaging sonar and its sonar image.

$$P_{3D} = \begin{bmatrix} X_{3D} \\ Y_{3D} \\ Z_{3D} \end{bmatrix} = \begin{bmatrix} r\cos\theta\cos\phi \\ r\sin\theta\cos\phi \\ r\sin\phi \end{bmatrix}. \quad (1)$$

The 2D point $P_{2D}$ $(x_{2D}, y_{2D})$ projected on the sonar image plane is expressed as follows:

$$P_{2D} = \begin{bmatrix} x_{2D} \\ y_{2D} \end{bmatrix} = \frac{1}{\cos\phi} \begin{bmatrix} X_{3D} \\ Y_{3D} \end{bmatrix} = \begin{bmatrix} r\cos\theta \\ r\sin\theta \end{bmatrix}. \quad (2)$$

Thus, in the 2D sonar images, the information of the elevation angle ($\phi$) is missing, and therefore the height information of the observed area cannot be discerned.

## 3. PROPOSED METHOD

We propose a 3D mapping method for an AUV using a single imaging sonar. The proposed method has two main processes: 2D sonar image registration and 3D point cloud generation, as shown in Fig. 2. The 2D mosaic image of sequential sonar images can provide 2D shape and intensity information over a wide range but without height information. In contrast, the 3D point cloud generated by the imaging sonar provides partial 3D information but has sparse points and a rough 3D shape. Thus, the two methods can complement each method's demerits. By fusing the two methods, a precise 3D mapping of the underwater environment can be performed; moreover, the AUV trajectory can be estimated.

### 3.1. 2D sonar image registration

We used a frequency-analysis-based method, and not a feature-based method, to register successive sonar image as shown in Fig. 3. Compared with optical images, sonar images have difficulties in extracting features because they have no color information and have few distinctive edges.

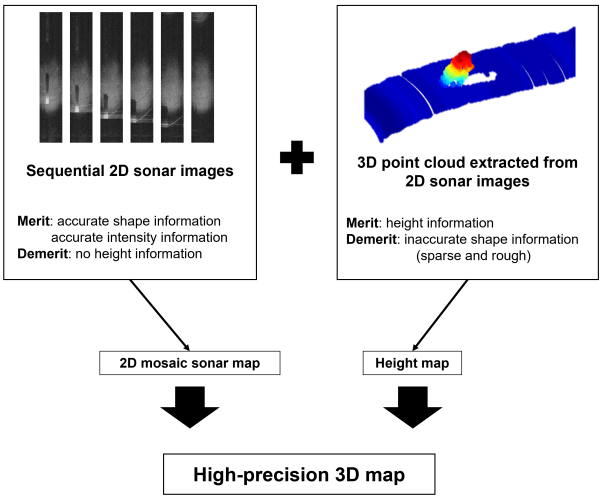


Fig. 2. Complementary fusion using 2D sonar image sequence and 3D point cloud.

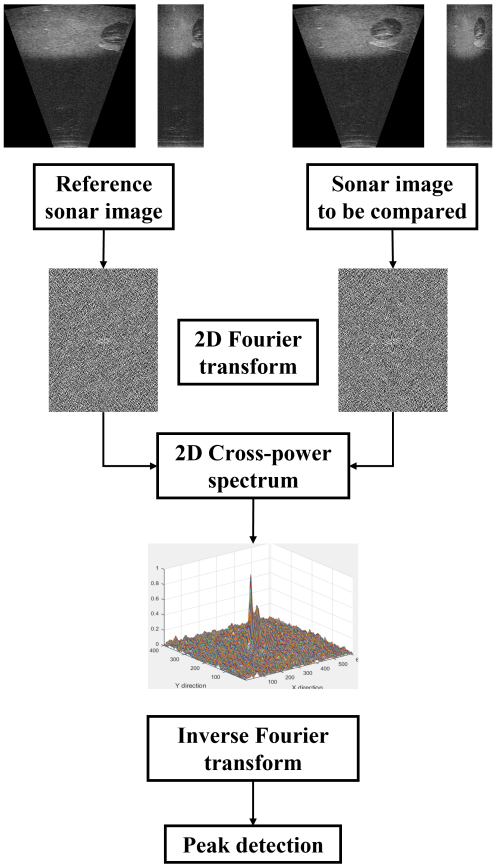


Fig. 3. Flowchart of the Fourier-based sonar image analysis method.

The frequency analysis method uses the Fourier transform to estimate the displacement and rotation of an AUV.

Let $i_r(m,n)$ and $i_c(m,n)$ be a reference sonar image and a sonar image to be compared, respectively. If two sonar images have a difference in pixel displacement of $(\Delta m, \Delta n)$, then the relationship between two sonar images can be expressed as

$$i_r(m,n) = i_c(m-\Delta m, n-\Delta n). \tag{3}$$

The 2D Fourier transforms of the two sonar images are then denoted as $I_r(u,v)$ and $I_c(u,v)$. From (3), $I_r(u,v)$ and $I_c(u,v)$ have the following relationship

$$I_r(u,v) = I_c(u,v)e^{-j(u\Delta m + v\Delta n)}. \tag{4}$$

From (4), it can be observed that the magnitudes of the 2D Fourier transform of the two sonar images are equal. Therefore, only the phase difference is analyzed to extract $\Delta m$ and $\Delta n$. The 2D cross-power spectrum function is used to express the phase term and is described as follows [23]:

$$P(u,v) = \frac{I_r(u,v)\,I_c^*(u,v)}{|I_r(u,v)\,I_c^*(u,v)|} = e^{-j(u\Delta m + v\Delta n)}, \tag{5}$$

where $I^*$ denotes the complex conjugate of $I$, and $P(u,v)$ denotes the phase correlation matrix. From (5), the displacement $(\Delta m, \Delta n)$ can be derived using a 2D inverse Fourier transform. In the ideal case, the 2D inverse Fourier transform of $P(u,v)$ corresponds to the 2D impulse function centered on $(\Delta m, \Delta n)$. However, in an actual scenario, nonzero values exist due to noise in the sonar images. As a result, the displacement $(\Delta m, \Delta n)$ can be determined using the peak detection method or a thresholding method.

The results of calculating displacement and rotation between two sonar images are used to mosaic the two images. After translating and rotating one sonar image based on another sonar image, the two sonar images can be stitched together to form a single mosaic image. Subsequently, the pixel values of two sonar images are averaged to perform the blending process. However, to prevent excessive pixel overlapping, the maximum number of overlaps is clipped for each pixel.

### 3.2. Displacement and rotation estimation

Two types of sonar images, fan-shaped and rectangular images, can be used to calculate the displacement and rotation of the AUV. Each pixel of the fan-shaped sonar image is represented in Cartesian coordinates. Each pixel in the rectangular sonar image is represented in polar coordinates. Therefore, the pixel displacement $(\Delta m, \Delta m)$ on the fan-shaped sonar image can be converted to the actual displacement movement $(\Delta x, \Delta y)$ of the AUV, as shown in Fig. 4(a). In addition, the pixel displacement $(\Delta n)$ in the azimuth direction $(\theta)$ on the rectangular sonar image can be converted to the actual yaw rotation $(\Delta\theta)$ of the AUV, as shown in Fig. 4(b). The differences calculated in pixels are converted to the actual AUV displacement and rotation values using the altitude of the AUV, tilt angle of the imaging sonar, maximum range, and minimum range of the imaging sonar. Therefore, by comparing the sonar image obtained at the current frame with the sonar image of the previous frame, we can estimate the heading angle and position change of the AUV.

However, the rotation cannot be accurately estimated by this approach because the displacement in the Cartesian coordinates causes distortions in the polar coordinate. The displacement and rotation of the AUV are coupled, so they affect each other. Nevertheless, if the sonar image's pixel displacement is relatively small compared to the size of the sonar image, then the distortions in the polar coordinate can be ignored. If a time interval is set to involve a sufficiently small drift error, this approach can be used to estimate the rotation of the AUV.

### 3.3. Height map generation

The height of the object at the point hit by the acoustic beam is related to the elevation angle. However, the elevation angle in a sonar image is lost because of the projection mechanism between the 3D scene and the 2D image.

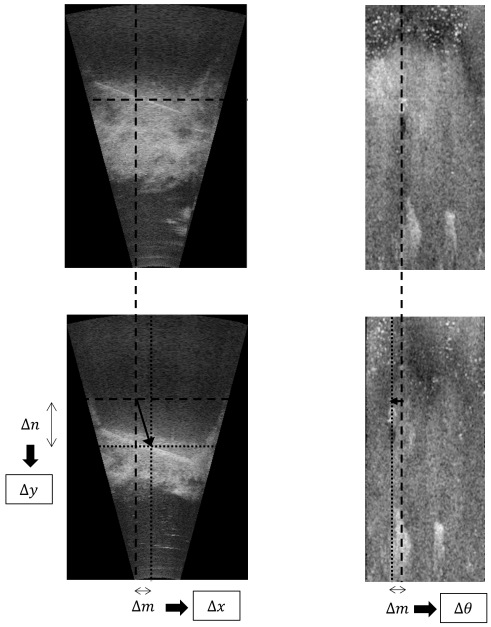


(a) Fan-shaped sonar images when pure displacement occurred (b) Rectangular sonar images when pure rotation occurred

Fig. 4. Changes in sonar images in pure displacement and pure rotation cases.

Thus, we were unable to measure the height of the object on the seafloor by using a single sonar image. This problem can be solved by utilizing the mobility of the AUV and changing the highlighted parts of the sonar images.

When the imaging sonar moves over the object on the seafloor, the length and location of the highlighted and shadowed parts of the sonar image change. During the forward movement of the imaging sonar, The highlighted part of the object protrudes in front of the shortest line of the seafloor on the sonar image. This phenomenon occurs because the shortest distance from the imaging sonar to the object with height is shorter than the shortest distance to the seafloor. We defined this phenomenon as the "highlight extension effect (HEE)" [20].

Depending on the height of the object, the highlight extending length is changed. The height profile for the object's protruded points can be estimated by analyzing the geometric relationship between the object on the seafloor and the imaging sonar.

For an object on the seafloor, critical points are defined as the shortest distance points where the imaging sonar's acoustic beams are reflected on the object. The critical point is generated for each acoustic beam. As shown in Fig. 5, the critical point position in the $j$th acoustic beam is expressed as $r_{cp}$ and $\theta_{cp}$ by using the imaging sonar's local coordinates. The local coordinates of the critical points can be calculated by

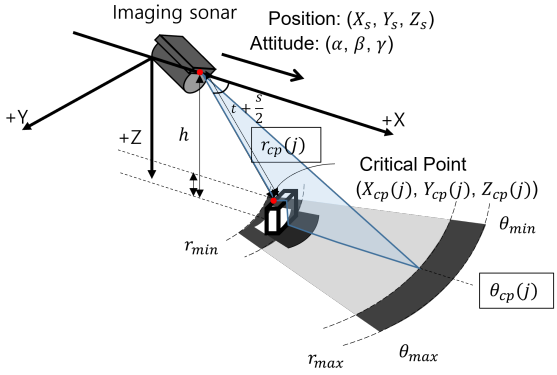


Fig. 5. A method for estimating the height of an object from the forward movement of an imaging sonar. The height profile is calculated by extracting the critical points for each path of the acoustic beam.

$$\begin{bmatrix} X_{cp}^{Local}(j) \\ Y_{cp}^{Local}(j) \\ Z_{cp}^{Local}(j) \end{bmatrix} = \begin{bmatrix} r_{cp}(j)\sqrt{1-\sin^2(t+\frac{s}{2})-\sin^2(\theta_{cp}(j))} \\ r_{cp}(j)\sin(\theta_{cp}(j)) \\ r_{cp}(j)\sin(t+\frac{s}{2}) \end{bmatrix}, \tag{6}$$

where $t$ and $s$ are the tilt angle and spreading angle of the imaging sonar, respectively. Because the imaging sonar is tilted by an angle, $t$, the azimuth angle, $\theta_{cp}(j)$, of the imaging sonar differs from the azimuth angle of the spherical coordinate. Therefore, $X_{cp}^{Local}(j)$ is calculated using $Y_{cp}^{Local}(j)$ and $Z_{cp}^{Local}(j)$. The position of the critical point in the global coordinates can be expressed using the rotation matrix, $\mathbf{R} = R_z R_y R_x$, and the position of the imaging sonar, $(X_s, Y_s, Z_s)$, can be represented by

$$\begin{bmatrix} X_{cp}(j) \\ Y_{cp}(j) \\ Z_{cp}(j) \end{bmatrix} = \begin{bmatrix} X_s \\ Y_s \\ Z_s \end{bmatrix} + \mathbf{R} \begin{bmatrix} X_{cp}^{Local}(j) \\ Y_{cp}^{Local}(j) \\ Z_{cp}^{Local}(j) \end{bmatrix}, \tag{7}$$

where $\mathbf{R}$ is a 3D rotation transformation matrix, which is determined from the roll angle, pitch angle, and yaw angle of the imaging sonar.

We could generate a 3D point cloud of the underwater object by accumulating the height profile of the object during the fly-by sonar motion, as shown in Fig. 6.

### 3.4. Fusion of 2D sonar map and height map

When an AUV equipped with an imaging sonar moves and acquires a sonar image sequence, the 2D sonar image registration and 3D point cloud generation are processed simultaneously. A height map was generated from the 3D point cloud. The 3D point cloud contains the information on the height of a partial area, and not the height of the entire sonar image. In particular, the height of the shadow part of the object cannot be measured. Therefore, the distance value of the seafloor from the sensor mounted on the AUV is used as the default seafloor level. The height value

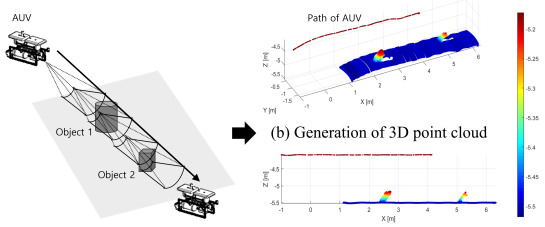


(a) Fly-by motion of AUV (c) Side view of the 3D point cloud

Fig. 6. Generation of 3D point cloud by AUV forward scans.

of the points estimated by the 3D point cloud is updated. A 3D sonar map can be generated by adding the height map information to the 2D mosaic sonar map.

## 4. EXPERIMENT & RESULT

### 4.1. Experimental setup

We conducted an indoor water tank experiment to verify the proposed method. As shown in Fig. 7(a), a hovering-type AUV 'Cyclops' was used, which was equipped with a Doppler velocity log (DVL), fiber-optic gyro (FOG), pressure sensor and imaging sonar [24]. The used imaging sonar was 'DIDSON', which is one of the forward scan sonar [25]. The detailed specifications of the DIDSON are described in Table 1.

This AUV is designed considering the stability of roll motion and pitch motion and installed four thrusters on the side for the independence between yaw motion and sway motion. The horizontal velocity of the AUV is measured from DVL, and the depth is measured from a pressure sensor.

We installed several types of objects on the floor of the water tank, as shown in Fig 7(b). All objects were relatively small with a length, width, and height of less than 1 m and varied in surface material and shape. We used the AUV to scan objects by moving along the lawnmower trajectory. The proposed method requires that the AUV speed should be sufficiently slow to produce larger over-

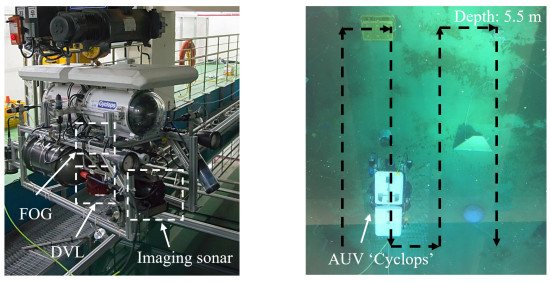


(a) Hovering type AUV 'Cyclops' (b) Experiment scene

Fig. 7. Experimental setup.

Table 1. Specifications of the imaging sonar (DIDSON) used in the experiment.

| | |
|---|---|
| Operating frequency | 1.8 MHz |
| Number of beams | 96 |
| Spreading angle | 14 ° |
| Field of view | 29 ° |
| Beam spacing | 0.3 ° |
| Range | 0.4 - 10 m |
| Frame rate | 4 - 21 fps |

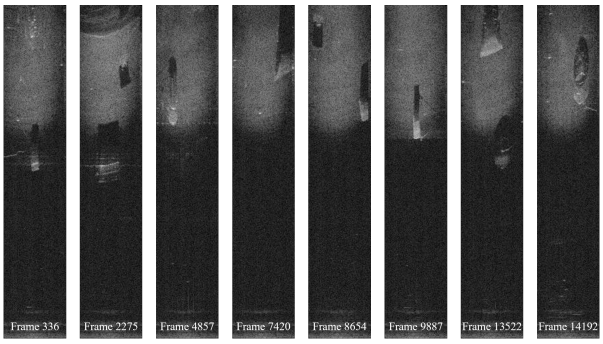


Fig. 8. Examples of sonar images acquired in the experiment.

lap areas between successive sonar image pairs. In addition, when generating a 3D point cloud, height profiles must be accumulated with a sufficiently large number of points. Thus, we adjusted the speed of the AUV to avoid being too fast. The depth of the AUV was 3 m, the altitude was about 2.48 m, and the roll and pitch angles were close to zero. It was also assumed that the floor of the water tank was flat. The imaging sonar was set to have a tilt angle of $t = 30°$ and spreading angle of $s = 14°$, minimum and maximum ranges of 0.83 m and 5.83 m, respectively. All of the sonar images acquired in the experiment were 14466 frames. Fig. 8 shows some of the acquired sonar images.

### 4.2. Results

The pixel size of the sonar image of DIDSON is 512 by 96, and the minimum pixel displacement that can be measured with a Fourier-based method is 1 pixel. Therefore, the displacement of AUV that can be estimated using a pair of sonar images has a minimum value. In this experiment, the displacement of AUV per pixel of the fan-shaped sonar image is 0.013 m and 0.01 m in the surge and sway directions, respectively. In addition, the amount of rotation of AUV per pixel of a rectangular sonar image is 0.3 °.

Since the DIDSON was operated fast at 10 fps, the displacement and rotation per frame of the AUV can be smaller than the minimum displacement and rotation that

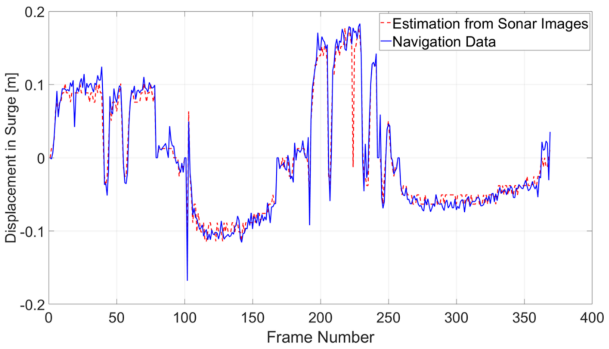


(a) Displacement in surge.

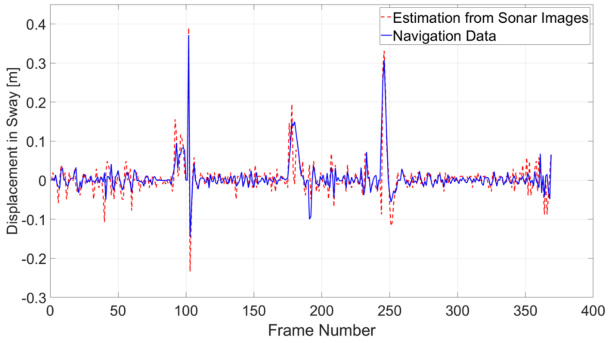


(b) Displacement in sway.

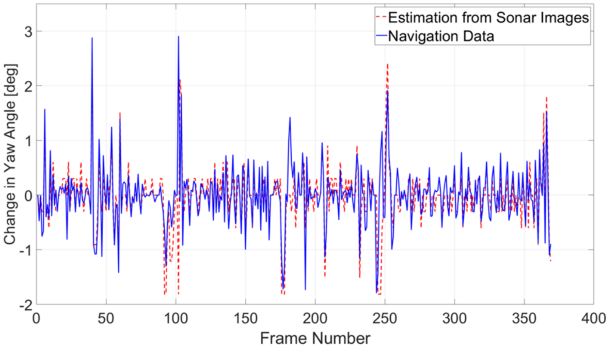


(c) Change in yaw angle.

Fig. 9. Comparison result about estimated displacement and rotation of AUV using the sonar image sequence.

can be estimated from the sonar image pairs. If all the frames of the sonar image sequence are used pairwise, some pairs are difficult to estimate the amount of displacement and rotation of the AUV. Therefore, we applied the proposed method using 1 frame per 40 frames, not all frames. That is, a total of 369 frames were used.

The displacement and rotation of the AUV were estimated using a sequence of 369 sonar images. Figs. 9(a) and 9(b) compare the estimated displacement in surge and sway direction with navigation data by analyzing the sonar image pairs using a Fourier-based method. As the AVU moved along the lawnmower trajectory as shown in Fig. 7(b), the AUV's velocity changes in the surge direction can be checked by displacement at each frame number. Since the AUV moved forward in the frame number between 1 and 80 and between 190 and 240, displacement in the surge mostly has positive values. Since the AUV moved backward in the frame number between 100 and 170 and between 250 and 360, displacement in the surge mostly has negative values. In the rest of the intervals, the AUV moved left and right in the sway direction, the displacement in the surge is close to 0. In addition, the displacement estimated only with the sonar image was in agreement with the trend of the DVL data, and the average error was about 0.011 m.

In the sway direction, the AUV moved to the right 3 times with the lawnmower trajectory, so there were 3 peaks on the positive side of the displacement. Similar to the displacement in the surge direction, the displacement in the sway estimated only with the sonar image was in agreement with the DVL data trend, and the average error was about 0.018 m. During the experiment, the yaw angle of the AUV was controlled not to move as much as possible. However, there was a slight change at the point where the sway movement was. The change in yaw angle estimated only with sonar images was in agreement with the trend of the FOG data, and the average error was about 0.26 °.

Fig. 10 shows the result of estimating the trajectory of the AUV. Navigation data on the blue line results from dead reckoning using the values measured using DVL and FOG. The red dotted line is the trajectory estimated using only the sonar image. Unlike DVL and FOG, the pressure sensor does not have accumulated error over time, so it was used equally as z values for both data. The trajectory estimated using only the sonar image moved less in both the surge direction and the sway direction than the trajectory estimated with the navigation data. Also, the entire trajectory rotated counterclockwise. However, as for the shape of the entire trajectory, the trends in the two data were in agreement.

Based on the estimated trajectory of the AUV, 2D sonar images were registered to create a 2D mosaic sonar map for the tank floor about 8.75 m by 5.9 m. As shown in Fig. 11, a 2D mosaic sonar map based on navigation data was compared with a 2D mosaic sonar map based on the trajectory estimated by the proposed method. Part 1 area represents the vertical wall of the tank. It can be seen that Fig. 11(a) showed a straight line, while Fig. 11(b) showed a misaligned image due to a trajectory error. The areas of Part 2, Part 3, and Part 4 were aluminum cylinders, concrete bricks, and sphere-shaped plastic container, respectively. Fig. 11(a) showed the shape of one object, while Fig. 11(b) showed a blurred image and the shape of multiple objects. Because the drift errors are accumulated in the navigation data, so the sonar image is not correctly registered.

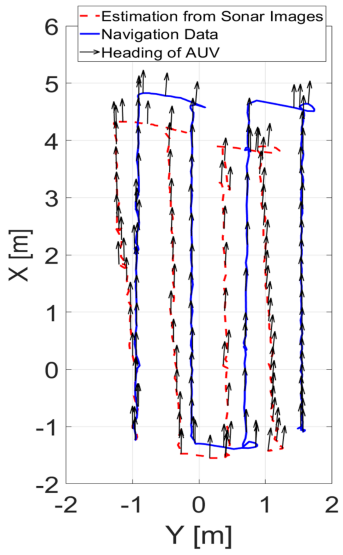


(a) Top view.

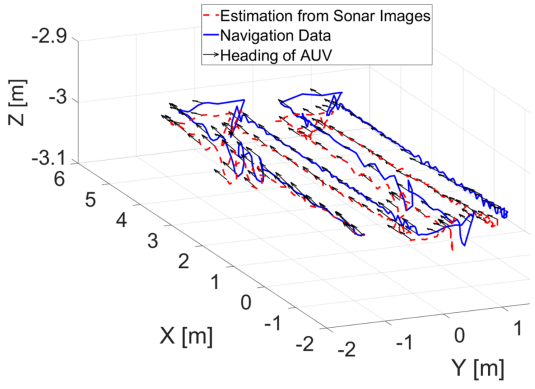


(b) 3D view.

Fig. 10. Estimation of AUV trajectory.

The height map generated by the proposed method is shown in Fig. 12(a). The critical points that occurred HEE in the sonar image sequence were detected, and the height profile was calculated. Since the AUV did not scan in the back or side direction of the object, the 3D point cloud was created incompletely, and the height map was also not perfect. A 3D sonar map generated by the fusion of two types of maps, which are 2D mosaic sonar map and height map, is shown in Fig. 12(b).

Fig. 13 shows the detailed results of the generated 3D sonar map. For each object, the actual size CAD model was placed at the corresponding location, and the length, width, and height were compared. Except for the Concrete brick 1 result in Fig. 13(b), the height of other objects were similar to the actual height. Although the shape of the object was not reconstructed to be completely distinguishable, we confirmed that each object's dimensions were similar. We verified that it is possible to generate a 3D sonar map including intensity information and shape information using the proposed method.

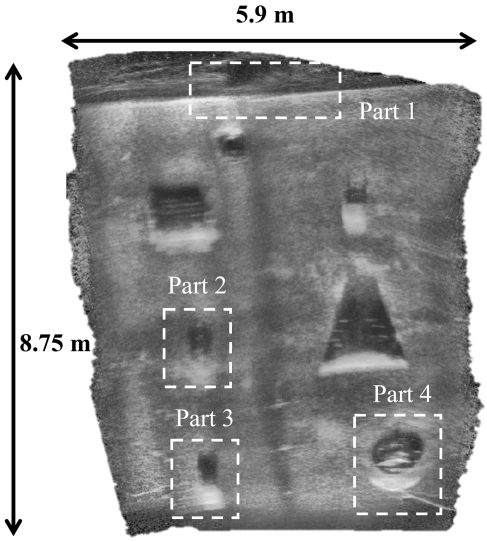


(a) Sonar image based.

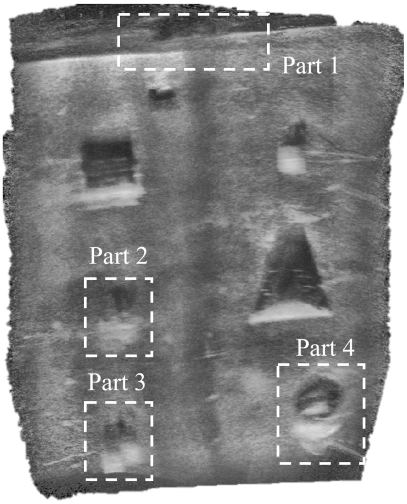


(b) Navigation data based.

Fig. 11. 2D mosaic sonar map of the floor of indoor water tank.

Table 2 shows a quantitative comparison of the 3D reconstruction results of each object. We measured the actual size of each object on the ground and used it as the ground truth value. Also, we measured the size of the reconstructed object shape in the 3D sonar map and used it as an estimation value. As a result, all objects' height except Concrete Brick 1 was estimated to be within 5 cm error. Concrete Brick 1 was installed on the floor using a long rope tied to the left and right. In the sonar image of Concrete Brick 1, a strong highlight part caused by the rope occurred in the horizontal direction. This is called crosstalk noise, a phenomenon in which an imaginary horizontal highlight line is created near a pixel with a strong highlight. Studies have been conducted to detect and remove crosstalk noise using a neural network-based algo-

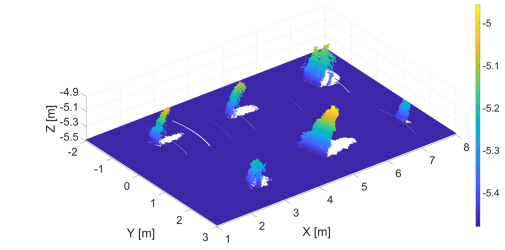


(a) Height map.

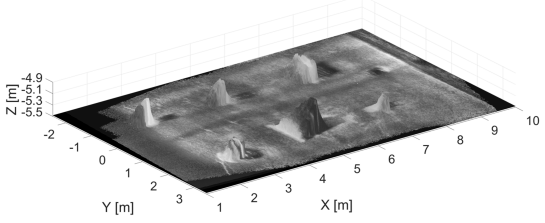


(b) 3D sonar map.

Fig. 12. Height map and 3D sonar map generated by 3D point cloud.

Table 2. Quantitative comparison of 3D reconstruction results of objects.

| Object | | L [m] | W [m] | H [m] |
|---|---|---|---|---|
| **Plastic Basket** | Actual Size | 0.62 | 0.38 | 0.34 |
| | Estimation | 0.78 | 0.68 | 0.39 |
| **Concrete Brick 1** | Actual Size | 0.19 | 0.15 | 0.39 |
| | Estimation | 0.31 | 0.19 | 0.25 |
| **Aluminum Cylinder** | Actual Size | 0.27 | 0.27 | 0.40 |
| | Estimation | 0.35 | 0.48 | 0.42 |
| **Tilted Wood Plate** | Actual Size | 0.70 | 0.50 | 0.50 |
| | Estimation | 0.74 | 0.73 | 0.52 |
| **Concrete Brick 2** | Actual Size | 0.19 | 0.15 | 0.39 |
| | Estimation | 0.29 | 0.41 | 0.42 |
| **Sphere-shaped Plastic Container** | Actual Size | 0.46 | 0.40 | 0.30 |
| | Estimation | 0.58 | 0.56 | 0.32 |

rithm [26]. The removal of crosstalk noise can improve the 3D reconstruction result.

In addition, the length and width of the object showed a large error. In particular, the width has the largest error due to the limitation of the 3D point cloud generation method. In the 3D point cloud generation method, HEE is analyzed from a sequential sonar image. The object's 3D point is created for every frame where HEE occurs, not just the frame where the maximum HEE occurs. Therefore, an incorrect 3D point cloud with an inclined surface is additionally created on the object's front surface. This phenomenon increased the width of the object. If the incorrect 3D point that does not overlap with the object's 2D shape is removed, the 3D reconstruction result can be improved.

## 5. CONCLUSION

We proposed a method for generating a precise underwater 3D map using an imaging sonar mounted on an AUV. Sonar image sequences obtained from the imaging sonar were analyzed using Fourier analysis in a frame-by-frame manner and were used to extract displacement and rotation information. The displacement and rotation estimated from the sonar image pairs were used to register the sonar images. Moreover, a method of obtaining a height map by generating a 3D point cloud from the sonar image sequences was presented. The 3D point cloud generation method cannot estimate the height of the entire sonar image, but can only estimate the height of one point for each acoustic beam of the imaging sonar. Therefore, the height map was generated by accumulating the 3D point cloud according to the imaging sonar's movement. The two maps, the 2D mosaic sonar map and the height map, were fused into a 3D seafloor map. We experimentally verified the proposed method in an indoor water tank. A 2D mosaic sonar map and a height map of the indoor tank with various objects on the floor were generated, and a 3D map was generated. In the future, the proposed method can be used with dead reckoning data to correct the AUV's drift error.

## REFERENCES

[1] J.-H. Kim, Y.-Z. Yoon, S.-C. Yu, and D.-J. Kang, "Real-time 2D height mapping method for an unmanned vehicle using a stereo camera and laser sensor fusion," *International Journal of Control, Automation and Systems*, vol. 10, no. 4, pp. 761-771, 2012.

[2] M. Sualeh and G.-W. Kim, "Simultaneous localization and mapping in the epoch of semantics: A survey," *International Journal of Control, Automation and Systems*, vol. 17, no. 3, pp. 729-742, 2019.

[3] S.-M. Lee, J. Jung, and H. Myung, "Geomagnetic field-based localization with bicubic interpolation for mobile robots," *International Journal of Control, Automation and Systems*, vol. 13, no. 4, pp. 967-977, 2015.

[4] W. Jeong, J. Moon, and B. Lee, "Error improvement in visual odometry using super-resolution," *International Journal of Control, Automation and Systems*, vol. 18, no. 2, pp. 322-329, 2020.

[5] V. Rosas-Cervantes and S.-G. Lee, "3D localization of a mobile robot by using Monte Carlo algorithm and 2D features of 3D point cloud," *International Journal of Control, Automation and Systems*, vol. 18, no. 11, pp. 2955-2965, 2020.

[6] B. Bingham, B. Foley, H. Singh, R. Camilli, K. Delaporta, R. Eustice, A. Mallios, D. Mindell, C. Roman, and D. Sakellariou, "Robotic tools for deep water archaeology: Surveying an ancient shipwreck with an autonomous underwater vehicle," *Journal of Field Robotics*, vol. 27, no. 6, pp. 702-717, 2010.

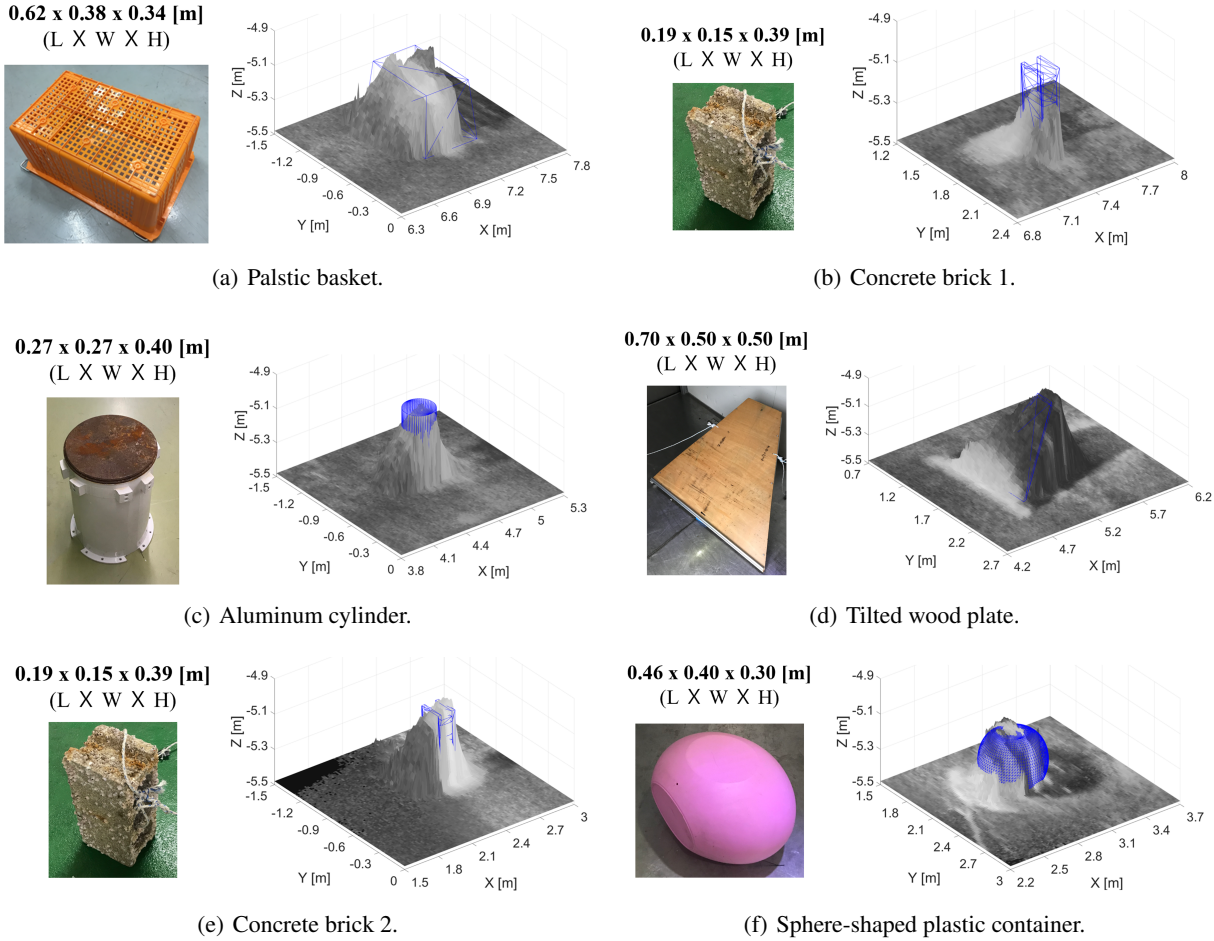


(a) Palstic basket. (b) Concrete brick 1.

(c) Aluminum cylinder. (d) Tilted wood plate.

(e) Concrete brick 2. (f) Sphere-shaped plastic container.

Fig. 13. Comparison of detailed results for each object in the 3D sonar map. The blue skeleton is the CAD model of each object placed at the actual scale.

[7] T. Kim, J. Kim, and S.-W. Byun, "A comparison of nonlinear filter algorithms for terrain-referenced underwater navigation," *International Journal of Control, Automation and Systems*, vol. 16, no. 6, pp. 2977-2989, 2018.

[8] D. Park, W. K. Chung, and J. Kim, "Analysis of electromagnetic waves attenuation for underwater localization in structured environments," *International Journal of Control, Automation and Systems*, vol. 18, no. 3, pp. 575-586, 2020.

[9] T. Maki, H. Mizushima, H. Kondo, T. Ura, T. Sakamaki, and M. Yanagisawa, "Real time path-planning of an AUV based on characteristics of passive acoustic landmarks for visual mapping of shallow vent fields," *Proc. of OCEANS 2007*, IEEE, pp. 1-8, 2007.

[10] B. Kim, J. Kim, M. Lee, M. Sung, and S.-C. Yu, "Active planning of AUVs for 3D reconstruction of underwater object using imaging sonar," *Proc. of IEEE/OES Autonomous Underwater Vehicle Workshop (AUV)*, IEEE, pp. 1-6, 2018.

[11] R. Garcia, J. Batlle, X. Cufi, and J. Amat, "Positioning an underwater vehicle through image mosaicking," *Proceedings of ICRA. IEEE International Conference on Robotics and Automation (Cat. No. 01CH37164)*, vol. 3, IEEE, pp. 2779-2784, 2001.

[12] J. Pyo, H.-G. Joe, J.-H. Kim, A. Elibol, and S.-C. Yu, "Development of hovering-type AUV "cyclops" for precision observation," *Proc. of OCEANS-San Diego*, IEEE, pp. 1-5, 2013.

[13] S. Hong and J. Kim, "Three-dimensional visual mapping of underwater ship hull surface using piecewise-planar slam," *International Journal of Control, Automation and Systems*, vol. 18, no. 3, pp. 564-574, 2020.

[14] S.-C. Yu, T.-W. Kim, A. Asada, S. Weatherwax, B. Collins, and J. Yuh, "Development of high-resolution acoustic camera based real-time object recognition system by using autonomous underwater vehicles." *Proc. of OCEANS 2006*, IEEE, pp. 1-6, 2006.

[15] M. Sung, J. Kim, M. Lee, B. Kim, T. Kim, J. Kim, and S.-C. Yu, "Realistic sonar image simulation using deep learning for underwater object detection," *International Journal of Control, Automation and Systems*, vol. 18, no. 3, pp. 523-534, 2020.

[16] S. Degraer, G. Moerkerke, M. Rabaut, G. Van Hoey, I. Du Four, M. Vincx, J.-P. Henriet, and V. Van Lancker, "Very-

high resolution side-scan sonar mapping of biogenic reefs of the tube-worm lanice conchilega," *Remote Sensing of Environment*, vol. 112, no. 8, pp. 3323-3328, 2008.

[17] S. Reed, I. T. Ruiz, C. Capus, and Y. Petillot, "The fusion of large scale classified side-scan sonar image mosaics," *IEEE Transactions on Image Processing*, vol. 15, no. 7, pp. 2049-2060, 2006.

[18] J. Vaganay, M. Elkins, D. Esposito, W. O'Halloran, F. Hover, and M. Kokko, "Ship hull inspection with the hauv: Us navy and nato demonstrations results," *Proc. of OCEANS 2006*, IEEE, pp. 1-6, 2006.

[19] S. Negahdaripour, P. Firoozfam, and P. Sabzmeydani, "On processing and registration of forward-scan acoustic video imagery," *Proc. of the 2nd Canadian Conference on Computer and Robot Vision (CRV'05)*, IEEE, pp. 452-459, 2005.

[20] H. Cho, B. Kim, and S.-C. Yu, "AUV-based underwater 3-D point cloud generation using acoustic lens-based multibeam sonar," *IEEE Journal of Oceanic Engineering*, no. 99, pp. 1-17, 2017.

[21] H. Joe, H. Cho, B. Kim, J. Pyo, and S.-C. Yu, "Profiling and imaging sonar fusion based 3D normal distribution transform mapping for AUV application," *Proc. of OCEANS-MTS/IEEE Kobe Techno-Oceans (OTO)*, IEEE, pp. 1-5, 2018.

[22] H. Joe, J. Kim, and S.-C. Yu, "3D reconstruction using two sonar devices in a Monte-Carlo approach for AUV application," *International Journal of Control, Automation and Systems*, vol. 18, no. 3, pp. 587-596, 2020.

[23] N. Hurtós, D. Ribas, X. Cufí, Y. Petillot, and J. Salvi, "Fourier-based registration for robust forward-looking sonar mosaicing in low-visibility underwater environments," *Journal of Field Robotics*, vol. 32, no. 1, pp. 123-151, 2015.

[24] J. Pyo, H. Cho, H. Joe, T. Ura, and S.-C. Yu, "Development of hovering type AUV "cyclops" and its performance evaluation using image mosaicing," *Ocean Engineering*, vol. 109, pp. 517-530, 2015.

[25] E. Belcher, W. Hanot, and J. Burch, "Dual-frequency identification sonar (didson)," *Proceedings of the 2002 International Symposium on Underwater Technology (Cat. No. 02EX556)*, IEEE, pp. 187-192, 2002.

[26] M. Sung, H. Cho, T. Kim, H. Joe, and S.-C. Yu, "Crosstalk removal in forward scan sonar image using deep learning for object detection," *IEEE Sensors Journal*, vol. 19, no. 21, pp. 9929-9944, 2019.

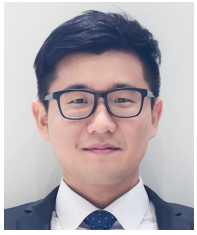

**Byeongjin Kim** received his B.E degree in electrical engineering from Pohang University of Science and Technology (POSTECH), Pohang, Korea in 2015. Currently, he is working toward a Ph.D. degree in the Department of Convergence IT Engineering at POSTECH, Pohang, Korea. He is a member of Hazardous and Extreme Environment Robotics (HERO) Lab in POSTECH. His research interests include underwater robotics, sonar image processing, and SLAM.

**Hangil Joe** received his B.S. degree in mechanical engineering in 2012 from Pusan National University, Busan, Korea, and an M.S. degree in ocean engineering in 2014 from Pohang University of Science and Technology (POSTECH), Pohang, Korea. He earned a Ph.D. degree in the Department of Convergence IT Engineering at POSTECH in 2019. In 2020, he joined the faculty of the Kyungpook National University, Daegu, Republic of Korea. He has been working in the areas of underwater robotics.

**Son-Cheol Yu** received his M.E. and Ph.D. degrees from the Department of Ocean and Environmental Engineering, University of Tokyo, in 2000 and 2003, respectively. He is an Associate Professor of the Department of Convergence IT Engineering, Electrical Engineering, and Advanced Nuclear Engineering with the Pohang University of Science and Technology (POSTECH), Korea. He is also the Director of Hazardous and Extreme Environment Robotics (HERO) Lab, IEEE Ocean Engineering Society Korea Chapter, Gyeongbuk Sea Grant Center. He has been a Researcher of mechanical engineering with the University of Hawaii from 2004 to 2007 and an Assistant Professor of mechanical engineering with the Pusan National University from 2008 to 2009. His research interest is Autonomous Underwater Vehicles, underwater sensing, and multi-agent-based robotics.